Canadian Science Publishing
NRC Research Press journals | Publishing Services

Canadian Geotechnical Journal
Revue canadienne de géotechnique

Modelling Deformation and Strains induced by Waste Settlement in a Centrifuge Test

Journal:	*Canadian Geotechnical Journal*
Manuscript ID	cgj-2017-0558.R1
Manuscript Type:	Article
Date Submitted by the Author:	22-Nov-2017
Complete List of Authors:	Yu, Yan; Queen's University, Civil Engineering Rowe, Kerry; Queen's University, Civil Engineering
Is the invited manuscript for consideration in a Special Issue? :	N/A
Keyword:	Geomembrane tensile strain;, Geosynthetic liner system, Landfill, Waste settlement, Geosynthetics

Modelling Deformation and Strains induced by Waste Settlement in a Centrifuge Test

Yan Yu[1] and R. Kerry Rowe[2]

1. Postdoctoral Fellow, GeoEngineering Centre at Queen's−RMC, Department of Civil Engineering, Queen's University, Kingston, ON K7L 3N6, Canada; E−mail: yan.yu@queensu.ca
2. Professor and Canada Research Chair in Geotechnical and Geoenvironmental Engineering, GeoEngineering Centre at Queen's−RMC, Department of Civil Engineering, Queen's University, Kingston, ON K7L 3N6, Canada; E-mail: kerry.rowe@queensu.ca

Abstract: A numerical model to estimate the tensile strains (loads) of the geomembrane liner in the waste containment facility due to waste settlement is presented. A centrifuge test of the geomembrane-lined landfill is used to validate the numerical model. The calculated surface settlement at the centre of the landfill and the geomembrane tensile strains on intermediate benches are generally in good agreement with the measured data. Parametric analyses associated with foundation shear strength, interface shear strength and stiffness, and geomembrane stiffness are performed. The influence of geometric nonlinearity on the geomembrane tensile strains is also examined. The numerical analyses indicate that the maximum geomembrane tensile strain occurs at the crest of the side slope near the intermediate bench for the cases and conditions examined. The lessons learned are likely to be useful to landfill design engineers using numerical models to aid in the design of the geosynthetic liner system for the waste containment facilities.

Key words: Waste settlement; Geomembrane tensile strain; Geosynthetic liner system; Waste containment facility; Numerical modeling; FLAC

1 Introduction

Modern waste containment facilities generally have a barrier system at the base of the facility to minimize the potential impacts of contaminants in the facilities on the surrounding environment and human health. Typically, a barrier system is comprised of two components (Rowe 2005; Rowe et al. 2014): (a) a highly permeable leachate collection system to collect and remove leachate for treatment and (b) a low permeability liner system to reduce the leachate leakage through the liner into groundwater and surface water. The performance of leachate collection systems in the field scale has been numerically examined by Rowe and Yu (2012, 2013b, 2013c) and Yu and Rowe (2013) using a sophisticated biogeochemical model (Yu and Rowe 2012) calibrated using laboratory mesocosm tests (Rowe and Yu 2013a). A practical design method was also proposed by Rowe and Yu (2013c) to estimate the service life and to optimize the design of leachate collection systems. Also much recent work has been done on the performance of geosynthetic clay liners (GCLs; e.g., Bannour et al. 2016; Chai et al. 2016; Malusis and Daniyarov 2016; Shackelford et al. 2016; Lu et al. 2017; Bouazza et al. 2017; Setz et al. 2017; Rowe et al. 2017; Saheli et al. 2017) and geomembranes (e.g., Abdelaal et al. 2014a; Gallagher et al 2016; Saheli and Rowe 2016; Yang et al. 2017; Kavazanjian et al. 2017; Rowe and Shoaib 2017; Eldesouky and Brachman 2018) including some on the interaction between the various components of the barrier system (Rentz et al. 2016; Rowe et al. 2016; McWatters et al. 2016; Touze-Foltz et al. 2016) and strains in the geomembrane associated with the leachate collection and protection layers (Rowe et al. 2013; Abdelaal et al. 2014a; Ewais et al. 2014). However, the performance of geosynthetic liner systems, and especially the strains induced in the geomembrane commonly used in the waste containment facilities due to waste settlement is still not well understood.

Based on field observations from the Kettleman Hills Landfill (a Class I hazardous waste treatment and storage facility in Kettleman City, California, USA), it was reported that the failure developed by sliding along interfaces of the underlying liner system beneath the waste fill and that this resulted in tears of the geomembrane liner on the side slopes during waste filling and a slope failure of the waste with lateral displacements of up to 10.7 m and surface settlements of up to 4.3 m (Mitchell et al. 1990). Factors influencing the performance of geosynthetic liner systems under waste which exhibits significant settlement with time include the interface shear strength between dissimilar materials, the stiffness and strength of each component in the geosynthetic liner system, and the thickness of waste lifts during waste filling. To understand the performance of geosynthetic liner systems below waste, field-scale tests are generally required. However, conducting field-scale tests are not feasible in most situations due to the major practical difficulties of doing so and the consequent cost and time needed to perform these tests.

An alternative to the field-scale testing is centrifuge modeling using scaled models and increasing the body stresses by centrifugal acceleration (e.g., Schofield 1980; Taylor 1995). Although the dimensions of the centrifuge model are scaled down from those of the prototype, the shear strength and unit weight together with the stress-strain relationship of materials from the prototype are kept unchanged in the centrifuge model. Thusyanthan et al. (2007) conducted the centrifuge study of tension in geomembranes on landfill slopes under both static and earthquake loading. Kavazanjian and Gutierrez (2017) reported a large-scale centrifuge test of the geomembrane-lined landfill with benches on side slopes similar to a typical canyon landfill subject to waste settlement and seismic loading. These centrifuge tests are very valuable in terms of improving our understanding of the performance of geosynthetic liner systems under field-

scale stress conditions. Although performing the centrifuge tests are more feasible than performing the field-scale tests, there is still very little published data from centrifuge tests addressing this issue. The design engineers must rely on other tools to estimate the performance of geosynthetic liner systems under waste settlement and to gain confidence when designing these systems.

Liu and Gilbert (2003) proposed a simplified method to calculate the geosynthetic loads in the liner system on side slopes during waste filling. While very useful for considering some loading conditions, this simplified method does not fully capture the interaction between the dissimilar materials and is unable to fully consider the waste settlement during and after waste filling. Numerical methods such as the finite element method (FEM) and finite difference method (FDM) are still the only practical tools available to aid in design of geosynthetic liner systems. Examples of the use of the FEM are Villard et al. (1999) and Filz et al. (2001), while Jones and Dixon (2005), Fowmes (2007), Fowmes et al. (2008), Arab (2011), Sia and Dixon (2012), Wu (2013), and Zamara et al. (2014) have used the FDM. While all of these cited papers have moved the field forward, the numerical models that have been validated using physical performance data are still limited to a simple landfill geometry. For example, Fowmes et al. (2008) developed a numerical modelling technique for a two-layered lining system (with a geomembrane liner and an overlying geotextile protection layer) on a vertical slope, and validated the model based on the measured relative interface shear displacements and geomembrane tensile loads at the anchorage from the large-scale laboratory tests. The magnitude of geomembrane (and geotextile) tensile strains and the influence of FLAC large- and small-strain modes on the numerical results were not reported by Fowmes et al. (2008). Furthermore, the numerical models associated with benches on side slopes reported by Fowmes (2007) and

Wu (2013) were not validated using physical testing results. Thus more research is needed in terms of development and validation of a numerical model using physical performance data at the end of waste placement from the field-scale and centrifuge tests with benches on side slopes for a typical canyon landfill, and to improve the understanding of the performance of geosynthetic liner systems subject to waste settlement.

The primary objective of this paper is to develop a numerical model using the FDM program FLAC (Itasca 2011) for a liner system in a waste containment facility subject to waste settlement and to validate the numerical model using physical performance data from a large-scale centrifuge test of the geomembrane-lined landfill (Kavazanjian and Gutierrez 2017) with benches on side slopes. The secondary objective is to use the numerical model to perform a parametric analysis of the effects of material and interface properties, and to examine the influence of FLAC large- and small-strain modes on the numerical results.

2 Centrifuge model

The centrifuge model examined in this paper was described in detail by Kavazanjian and Gutierrez (2017). The geometry of the centrifuge model cross section is shown in Figure 1. The foundation was simulated using the lightly cemented sand which was a mixture of Nevada sand and 4% Portland cement by weight (Kavazanjian and Gutierrez 2017). The waste was simulated using a 3:1 (by weight) peat-sand mixture (Kavazanjian and Gutierrez 2017). The geomembrane liner was a thin (0.051 mm) perfluorosulfonic acid (PFSA) membrane. To maximize the tension generated in the PFSA membrane, a thin low density polyethylene (LDPE) membrane was placed below the PFSA membrane on the side slopes. The top of the LDPE membrane was lubricated such that the interface shear strength between the PFSA membrane and the LDPE

membrane was negligible. The slopes on the left and right sides of the model had a horizontal to vertical ratio of 2H:1V and 1H:1V, respectively. The model was subjected to a centrifuge acceleration of 60 g (where g is the standard acceleration due to gravity). More details about the centrifuge model are provided by Kavazanjian and Gutierrez (2017).

3 Numerical model and parameter values

3.1 Prototype geometry and FDM numerical model

Figure 2 shows the prototype geometry and FDM numerical grid. The prototype for the centrifuge model at the 60 g acceleration had an maximum and minimum foundation thicknesses of 24 and 6 m, respectively. Both the left and right benches were 5 m wide. The maximum thickness of the waste was 31 m. The prototype dimension of the PFSA membrane used in the model was 3 mm. A total of 11240 zones (elements) were used for modelling the foundation and waste. The PFSA membrane was modeled using 374 beam elements with both left and right membrane ends anchored. Both left and right boundaries of the prototype were fixed in x direction only (smooth rigid). The bottom of the prototype was fixed in both x and y directions (rough rigid).

3.2 Cemented sand parameters

The cement sand was modeled using a nonlinear elastic-plastic model with Mohr-Coulomb failure criterion developed by Yu et al. (2016). The nonlinear elastic part of this model has a nonlinear elastic tangent modulus (E_t) and an unloading-reloading elastic modulus (E_{ur}) from Duncan et al. (1980) and a bulk modulus (B) from Selig (1988) as:

$$E_{\mathrm{t}} = \left[1 - \frac{R_{\mathrm{f}}(1 - sin\,\phi_{\mathrm{f}})(\sigma_1 - \sigma_3)}{2c_{\mathrm{f}}\cos\phi_{\mathrm{f}} + 2\sigma_3\,sin\,\phi_{\mathrm{f}}}\right]^2 K_{\mathrm{e}} p_{\mathrm{a}} \left(\frac{\sigma_3}{p_{\mathrm{a}}}\right)^n \quad (1)$$

$$E_{\mathrm{ur}} = K_{\mathrm{ur}} p_{\mathrm{a}} \left(\frac{\sigma_3}{p_{\mathrm{a}}}\right)^n \quad (2)$$

$$B = B_{\mathrm{i}} \left(1 + \frac{\sigma_{\mathrm{m}}}{B_{\mathrm{i}}\varepsilon_{\mathrm{u}}}\right)^2 \quad (3)$$

where R_{f} = failure ratio, ϕ_{f} = soil friction angle, σ_1 = major principle stress, σ_3 = minor principle stress, c_{f} = soil cohesion, K_{e} = soil elastic modulus number, p_{a} = atmospheric pressure, n = soil elastic modulus exponent, K_{ur} = unloading-reloading modulus number ($K_{\mathrm{ur}} = 1.2K_{\mathrm{e}}$; Duncan et al. 1980), B_{i} = initial tangent bulk modulus, ε_{u} = asymptotic value of the volumetric strain at large stresses, and σ_{m} = mean stress [i.e., $\sigma_{\mathrm{m}} = (\sigma_1 + \sigma_2 + \sigma_3)/3$], B_{i} and ε_{u} = intercept and inverse of the slope from a plot of $\sigma_{\mathrm{m}}/\varepsilon_{\mathrm{vol}}$ versus σ_{m}, respectively, in an isotropic compression test ($\varepsilon_{\mathrm{vol}}$ = volumetric strain).

Due to the restriction of the Poisson's ratio within 0-0.49 in this investigation, the range of the soil bulk modulus in Equation (3) is given as:

$$\frac{E_{\mathrm{t}}}{3(1 - 2v_{\mathrm{t,min}})} \leq B \leq \frac{E_{\mathrm{t}}}{3(1 - 2v_{\mathrm{t,max}})} \quad (4)$$

where $v_{\mathrm{t,min}}$ = minimum tangent Poisson's ratio ($v_{\mathrm{t,min}} = 0$ in this investigation), and $v_{\mathrm{t,max}}$ = maximum tangent Poisson's ratio ($v_{\mathrm{t,max}} = 0.49$ in this investigation).

The base case parameter values for the cemented sand are listed in Table 1. Figure 3 shows the measured and calculated stress-strain response of the cemented sand from the reported triaxial compression tests. Two sets of shear strength parameters (i.e., the friction angle and cohesion) were considered. The calculated stress-strain responses from the first set (i.e., $\phi_f = 34°$ and $c_f = 28$ kPa; the base case) of shear strength parameters agreed well with the triaxial tests at the confined pressures of $\sigma_3 = 100$ and 250 kPa, but over-predicted the triaxial results when $\sigma_3 = 500$ kPa. The second set ($\phi_f = 29°$ and $c_f = 18$ kPa) was taken from Kavazanjian and Gutierrez (2017) with good agreement between the calculated and measured data at $\sigma_3 = 500$ kPa, while under-predicted the measured data when $\sigma_3 = 100$ and 250 kPa.

Figure 4 shows the calculated and measured stress-strain responses of the cemented sand from one-dimensional (1D) compression tests. The two sets of shear strength parameters predicted the similar stress-strain responses under 1D compression conditions and over-estimated the axial strains for the vertical stress σ_1 between 10 and 100 kPa when compared with the measured data. It should be noted that even for the two 1D laboratory tests under the same testing conditions the differences in measured axial strains from Kavazanjian and Gutierrez (2017) were also observed.

3.3 Sand-peat mixture parameters

The sand-peat mixture was modeled (Table 2) using a modified Cam-Clay model available in FLAC constitutive model library. The calculated and measured stress-strain responses of the sand-peat mixture from one-dimensional compression test were in good agreement (Figure 5).

3.4 PFSA membrane parameters

Based on the laboratory tensile load tests (Kavazanjian and Gutierrez 2017), the PFSA membrane reached its tensile strength T_y = 2.0 kN/m at the tensile strain ε_y = 6% (Figure 6). The decrease in tensile load after reaching the peak value was not considered in this investigation. A linear elastic behaviour was considered in this paper for a tensile strain $\varepsilon < 6\%$ resulting a PFSA membrane stiffness $J = T_y/\varepsilon_y = 2.0/0.06 = 33.3$ kN/m (Figure 6; Table 3). Under the centrifuge acceleration 60 g, the membrane tensile strength and stiffness scale to $T_y = 2.0 \times 60 = 120$ kN/m and $J = 33.3 \times 60 = 2000$ kN/m at prototype scale (Table 3). The PFSA membrane was assumed to have no compressive stiffness and hence no stress when in compression. The moment of inertia was assumed to be zero (Table 3) for PFSA membrane beam elements.

3.5 Interface parameters

The interaction between the dissimilar materials was modeled using zero-thickness interface elements with base case properties given in Table 4. The friction angle between the geomembrane (PFSA membrane) and the waste (sand-peat mixture) was $\phi_{gw} = 27°$ (Kavazanjian and Gutierrez 2017). Kavazanjian and Gutierrez (2017) indicated that the friction angle between the geomembrane (PFSA membrane) and the foundation (cemented sand) was greater than that between the geomembrane (PFSA membrane) and waste (sand-peat mixture). The friction angle of the foundation (cemented sand) given by Kavazanjian and Gutierrez (2017) was $\phi_f = 29°$. The interface friction angle between the geomembrane (PFSA membrane) and the foundation (cemented sand) was assumed to be $\phi_{gf} = 29°$ (base case) based on $\phi_{gf} \leq \phi_f$. A lower friction angle $\phi_{gf} = 20°$ was also examined in the parametric study. The friction angle of the interface between the PFSA membrane and the HDPE membrane was taken to be $\phi_{gg} = 0$ because the top of the PFSA membrane was lubricated (Kavazanjian and Gutierrez 2017). No dilation and cohesion

strength were considered at any interface in this investigation (i.e., dilatancy angle $\psi_i = 0$ and cohesion $c_i = 0$). All interfaces had a normal stiffness value of $k_n = 100$ MPa/m and a shear stiffness value of $k_s = 1$ MPa/m based on Yu and Bathurst (2017). The influence of other interface normal and shear stiffness values on the numerical results were also examined. Zamara et al. (2014) numerically examined the performance of a geomembrane liner with an overlying geotextile protection layer in the field using both strain-softening and non-strain-softening interface models, and found that both interface models were unable to predict the measured geomembrane strains. They further suggested the use of a non-strain-softening interface model with reduced shear strength if the geosynthetics were exposed to the sun for an extended period of time. However, since strain softening was not anticipated in the centrifuge model test, the strain-softening behavior of geosynthetic interfaces (i.e., the displacement-dependent interface shear strength) was not modelled in this paper.

3.6 Modeling of centrifugal acceleration

The centrifuge model was prepared in a reduced scale and subjected to its own gravity initially (i.e., 1 g). The reduced-scale model was then accelerated to 60 g (Kavazanjian and Gutierrez 2017). The numerical modeling presented in this paper was performed for the prototype and hence full loading (1g) at prototype scale corresponds to 60g in the model test.

From the published papers, it appears that previous studies by Fowmes (2007), Fowmes et al. (2008) and Wu (2013) modelled the generation of down-drag load on the geomembrane in the laboratory and field using a full gravity loading approach (1g) when each waste layer was added to the model to simulate the waste settlement under its self-weight and external applied loading. Thus a difference between the previous modelling and that conducted here for a centrifuge acceleration of 60g was the need to adopt an incremental gravity loading procedure whereby

gravity in the prototype simulation was increased progressively 60 loading steps to 1g to capture the stress-path and nonlinear material behavior as well as possible. The first step was to activate the foundation and waste zones with linear elastic material models under g/60 where g = 10 kN/m^3 with material parameter values in Table 5. Also activated in the first step were the PFSA membrane beam elements. The model was then solved to reach the force equilibrium. Thereafter the foundation was modeled using a nonlinear elastic-plastic model (Table 1) and the waste was modeled using a Mohr-Coulomb model (Table 5). After the model reached the force equilibrium, the Cam-Clay model was applied to the waste (Table 2). In the next 59 loading steps, gravity was incremented by g/60 at each step until 1 g gravity in the prototype was achieved. Force equilibrium was reached at each step before moving to the next step. The use of the incremental gravity loading procedure in the prototype has been used by Zeng and Lim (2002) to model the centrifugal acceleration.

4 Numerical Results

4.1 Base case

The magnitude of the landfill surface settlements varies along the landfill top surface. As shown in Figures 1 and 2, the centrifuge model and corresponding porotype are non-symmetrical, and the centre of the landfill top surface is on the left side of the centre of the landfill base. The final deformed mesh under 1 g gravity in the prototype using the base parameter values and FLAC large-strain mode (Figure 7) corresponded to a calculated maximum surface settlement of 4.7 m at the landfill top surface vertically above the centre of the landfill base (see Figure 7). The calculated surface settlement at the centre of the landfill top surface was about 4.5 m (Figure 7), which was in reasonable agreement with the measured 4.2 m reported by Kavazanjian and

Gutierrez (2017). The modeling indicated that the foundation settlement was negligible and the waste settlement was due to the high compressibility of the waste itself.

As the waste settles, while the foundation remains practically unchanged, tensile loads and strains develop within the geomembrane (PFSA membrane). For the base parameters and using FLAC large-strain mode, the maximum tensile load and strain on either left or right side of the landfill occurred at the crest of the side slope near the intermediate bench (Figures 8 and 9). The calculated tensile loads of the PFSA membrane (Figure 9a) were near zero on the top left surface of the foundation and increased to between 0.8 and 22.2 kN/m on the upper left side slope. On the left intermediate bench, the calculated tensile loads were between 12.6 and 103.5 kN/m. The maximum calculated tensile load was about 120 kN/m (i.e., reaching the PFSA membrane peak tensile strength) at the crest of the lower left side slope. However, this doesn't mean that the PFSA membrane failed (or tore) during the physical test. The current numerical model does not consider a reduction in the tensile load after the PFSA membrane reaches the peak tensile load (i.e., the current model does not capture the post peak behavior evident in the physical test on the PFSA membrane shown in Figure 6). The calculated tensile loads of the PFSA membrane on the flat base were much less than the maximum tensile loads on the side slopes and of no practical concern in design. On the right side of the model there was a somewhat similar trend to the left side with the peak tensile strength of the PFSA membrane (120 kN/m) being reached at the crest of the lower right side slope. The calculated tensile loads were between 0 and 71.9 kN/m on the right intermediate bench and between 0 and 7.5 kN/m on the right upper side slope.

The calculated PFSA membrane strains (Figure 9b) were between 0.04% and 1.1% on the upper left side slope. On the left intermediate bench, the strains were estimated to be between

0.6 and 5.2% which bracketed the two measured stains of 4.5-4.6% reported by Kavazanjian and Gutierrez (2017). The calculated maximum tensile strain of 13.8% occurred at the crest of the lower left side slope (no reported measured data at this location). On the flat base, the calculated stains of the PFSA membrane were less than 0.7% were of no practical concern in terms of geomembrane strains. On the right side of the model, the calculated maximum strain was 12.2% at the crest of the lower right slope. The strains were calculated to be between 0 and 3.6% on the right intermediate bench which bracketed the measured strain of 3.3% (Kavazanjian and Gutierrez 2017). A higher measured strain value (4.7%) on the right bench was not considered in this paper because the settlement sensor above this strain gauge slipped from its seat (Kavazanjian and Gutierrez 2017) which may have interfered the strain gauge reading. The calculated strains on the upper right side slope were less than 0.4%. Thus for the case and conditions examined the maximum geomembrane tensile load and strain due to waste settlement occurred at the crest of the lower side slope near the intermediate bench on both sides of the waste containment facility.

Based on the data available form the centrifuge test it appears that the model gave encouraging agreement with observed behaviour.

4.2 Influence of foundation (cemented sand) parameter values

Figure 10a shows the influence of foundation (cemented sand) parameter values on the PFSA membrane tensile loads. The numerical results showed that the two sets of cemented sand parameter values considered in this investigation resulted in the similar distribution of the PFSA membrane tensile loads. For the PFSA membrane tensile strains as shown in Figure 10b, the maximum tensile strain was about 11.4% when using the cemented sand parameter values from

Kavazanjian and Gutierrez (2017) which was lower than 13.8% from the base case parameter values. The difference in maximum PFSA membrane tensile strain in Figure 10b was due to the different stress-strain responses of the two sets of cemented sand parameters shown in Figure 3. However, the two different sets of cemented sand parameter values predicted the similar tensile strains on each intermediate bench where measured data were available. The maximum tensile force was 120 kN/m in both cases because the geomembrane had yielded at 120 kN/m and was deforming plastically. As a similar situation exists in the cases below but will not be explicitly discussed.

4.3 Influence of interface shear strength between PFSA membrane and foundation (cemented sand)

Figure 11 shows the influence of interface shear strength between the PFSA membrane and foundation (cemented sand) on the PFSA membrane tensile loads and strains. The numerical analysis indicated that the PFSA membrane-foundation interface shear strength (ϕ_{gf}) between 20° and 29° had negligible influence on both the PFSA membrane tensile loads and strains.

4.4 Influence of interface normal and shear stiffness

The influence of interface shear stiffness on the PFSA membrane tensile loads and strains is shown in Figure 12. Increasing the interface shear stiffness value from k_s = 1 to 10 MPa/m slightly decreased the tensile loads and strains on the intermediate benches when other conditions were kept same. The maximum tensile strain was reduced from 13.8% to 12.9% when increasing the interface shear stiffness from k_s = 1 to 10 MPa/m (Figure 12b).

Figure 13 shows the influence of both interface shear and normal stiffness on the PFSA membrane tensile loads and strains. Increasing the interface shear stiffness from k_s = 1 to 100 MPa/m and normal stiffness from k_n = 100 to 1000 MPa/m resulted in a slight decrease in maximum tensile strain from 13.8% to 13.1% (Figure 13b).

The results from both Figures 12 and 13 indicated that the interface shear stiffness between k_s = 1 and 100 MPa/m and normal stiffness k_n = 100 to 1000 MPa/m can predict the similar tensile loads and strains for the case and conditions examined.

4.6 Influence of FLAC large- and small-strain mode

The influence of large- and small-strain mode on the PFSA membrane tensile loads and strains using base case parameter values is shown in Figure 14. The calculated strains on the left intermediate bench were between 1.2 and 4.3% when using the small-strain mode (versus calculated values between 0.6 and 5.2% using the large-strain mode and measured values of 4.5-4.6% from Kavazanjian and Gutierrez 2017). On the right intermediate bench, the calculated strains using the small-strain mode were between 0.02 and 3.25% (compared to calculated values between 0 and 3.6% using the large-strain mode and measured value of 3.3% from Kavazanjian and Gutierrez 2017). Figure 14b also shows that the calculated tensile strains near the centre of each bench were between the calculated minimum and maximum tensile strains on each bench. The strain measurements reported by Kavazanjian and Gutierrez (2017) were taken at the centre region of each bench. The numerical results also showed that the small-strain mode predicted higher tensile loads and strains on both left and right upper side slope than did the large-strain mode. However, the maximum tensile strain was 9.6% when using the small-strain mode which

was lower than 13.4% when using the large-strain mode. It is the maximum geomembrane tensile strain that is a practical concern when designing the geomembrane liner.

5 Conclusions

A numerical model was developed in this investigation using the finite different program FLAC (Itasca 2011) to predict the performance of a geomembrane liner subject to the waste settlement within a waste containment facility. The model was used to examine a large-scale centrifuge test of the geomembrane-lined landfill reported by Kavazanjian and Gutierrez (2017). Parametric analyses were performed regarding the foundation shear strength and the interface shear strength and stiffness. Both FLAC large- and small-strain modes were considered to examine the influence of geometric nonlinearity on geomembrane tensile strains. For the conditions and cases reported in this paper, it is concluded that:

- The calculated surface settlement at landfill centre and geomembrane tensile strains on the intermediate benches were in encouraging agreement with the measured data from the centrifuge test when using base case parameter values and FLAC large-strain mode.
- The calculated maximum geomembrane tensile strain occurred at the crest of the side slope near the intermediate bench.
- The estimated maximum geomembrane tensile strain from FLAC small-strain mode (without modelling geometric nonlinearity) was lower than that from FLAC large-strain mode.
- The numerical results show that the geomembrane with axial tensile stiffness J = 2000 kN/m (in the prototype) yielded and the maximum geomembrane tensile load reached the tensile strength T_y = 120 kN/m (in the prototype).

Acknowledgements

The work reported in this paper was supported by a grant A1007 from the Natural Sciences and Engineering Research Council of Canada (NSERC). The authors are extremely grateful to the two anonymous reviewers for their comments and suggestions which greatly helped improve the paper.

References

Abdelaal, F.B., Rowe, R.K., and Brachman, R.W.I. 2014a. Brittle rupture of an aged HDPE geomembrane at local gravel indentations under simulated field conditions. *Geosynthetics International*, 21 (1): 1-23.

Abdelaal, F.B., Rowe, R.K., and Islam, M.Z. 2014b. Effect of leachate composition on the long-term performance of a HDPE geomembrane. *Geotextiles and Geomembranes*, 42(4): 348-362.

Arab, M.G. 2011. The integrity of geosynthetic elements of waste containment barrier systems subject to seismic Loading. Ph.D. thesis. School of Sustainable Engineering and the Built Environment, Arizona State University, Tempe, Arizona, USA.

Bannour, H., Touze-Foltz, N., and Pierson, P. 2016. Transient hydraulic behavior of two GMBs–GCLs composite liners, *Geotextiles and Geomembranes*, 44(1): 51-58.

Boscardin, M.D., Selig, E.T., Lin, R.S., and Yang, G.R. 1990. Hyperbolic parameters for compacted soils. *ASCE Journal of Geotechnical Engineering*, 116 (1): 88–104.

Bouazza, A., Ali, M.A., Rowe, R.K., Gates, W.P., and El-Zein, A. 2017. Heat mitigation in geosynthetic composite liners exposed to elevated temperatures. *Geotextiles and Geomembranes*, 45(5): 406-417.

Chai, J.C., Sari, K., Shen, S.L., and Ca, Y.Q. 2016. Predicting self-healing ratio of GCL with a damage hole. *Geotextiles and Geomembranes*, 44(5): 761-769

Duncan, J.M., Byrne, P.M., Wong, K.S., and Mabry, P. 1980. Strength, stress-strain and bulk modulus parameters for finite element analyses of stresses and movements in soil masses. Report No. UCB/GT/80-01, Department of Civil Engineering, University of California, Berkeley, CA.

Eldesouky, H.M.G., and Brachman, R.W.I. 2018. Calculating local geomembrane strains from a single gravel particle with thin plate theory. *Geotextiles and Geomembranes*, 46(1): 101-110

Ewais, A.M.R., Rowe, R.K., Brachman, R.W.I., and Arnepalli, D.N. 2014. Service-life of a HDPE GMB under simulated landfill conditions at 85^{o}C. *ASCE Journal of Geotechnical and Geoenvironmental Engineering*, 140(11): 04014060.

Filz, G.M., Esterhuizen, J.J.B., and Duncan, J.M. 2001. Progressive failure of lined waste impoundments. *ASCE Journal of Geotechnical and Geoenvironmental Engineering*, 127(10): 841-848.

Fowmes, G.J. 2007. Analysis of steep sided landfill lining systems. Ph.D. thesis, Department of Civil and Building Engineering, Loughborough University, Loughborough, UK.

Fowmes, G.J., Dixon, N., and Jones, D.R.V. 2008. Validation of a numerical modelling technique for multilayered geosynthetic landfill lining systems. *Geotextiles and Geomembranes*, 26(2): 109-121.

Gallagher, E.M., Tonks, D.M., Shevelan, S., Belton, A.R., and Blackmore, R.E. 2016. Investigations of geomembrane integrity within a 25-year old landfill capping. *Geotextiles and Geomembranes*, 44(5): 770-780

Itasca, 2011. FLAC: Fast Lagrangian Analysis of Continua. Version 7.0 [computer program]. Itasca Consulting Group, Inc., Minneapolis, MN.

Jones, D.R.V., and Dixon, N. 2005. Landfill lining stability and integrity: the role of waste settlement. *Geotextiles and Geomembranes*. 23(1): 27-53.

Kavazanjian, E., and Gutierrez, A. 2017. Large scale centrifuge test of a geomembrane-lined landfill subject to waste settlement and seismic loading. *Waste Management*, 68: 252-262

Kavazanjian, E., Andresen, J., and Gutierrez, A. 2017. Experimental evaluation of HDPE geomembrane seam strain concentrations. *Geosynthetics International*, 24(4): 333–342.

Liu, C.N., and Gilbert, R.B. 2003. Simplified method for estimating geosynthetic loads in landfill liner side slopes during filling. *Geosynthetics International*, 10(1): 24–33.

Lu, Y., Abuel-Naga, H., and Bouazza, A. 2017. Water retention curve of GCLs using a modified sample holder in a chilled-mirror dew-point device. *Geotextiles and Geomembranes*, 45(1): 23-28

Malusis, M.A., and Daniyarov, A.S. 2016. Membrane efficiency and diffusive tortuosity of a dense prehydrated geosynthetic clay liner. *Geotextiles and Geomembranes*, 44(5): 719-730.

McWatters, R.S., Rowe, R.K., Wilkins, D., Spedding, T., Jones, D., Wise, L., Mets, J., Terry, D., Hince, G., Gates, W.P., Di Battista, V., Shoaib, M., Bouazza, A., and Snape, I. 2016. Geosynthetics in Antarctica: Performance of a composite barrier system to contain hydrocarbon-contaminated soil after 3 years in the field. *Geotextiles and Geomembranes*, 44(5): 673-685.

Mitchell, J.K., Seed, R.B., and Seed, H.B. 1990. Kettleman Hills waste landfill slope failure, I: liner system properties. *ASCE Journal of Geotechnical Engineering*, 116(4): 647–68.

Rentz, A., Take W.A., Brachman, R.W.I., and Rowe, R.K. 2016. Effect of geomembrane colour and cover soil on solar-driven down slope bentonite erosion from a GCL. *Geosynthetics International*, 23(4): 257–270.

Rowe, R.K. 2005. Long-term performance of contaminant barrier systems. *Géotechnique*, 55(9): 631-678.

Rowe, R.K., and Shoaib, M. 2017. Long-term performance HDPE geomembrane seams in MSW leachate. *Canadian Geotechnical Journal*, https://doi.org/10.1139/cgj-2017-0049

Rowe, R.K., and Yu, Y. 2012. Clogging of finger drain systems in MSW landfills. *Waste Management*, 32(12): 2342–2352.

Rowe, R.K., and Yu, Y. 2013a. Modelling of leachate characteristics and clogging of gravel drainage mesocosms permeated with landfill leachate. *ASCE Journal of Geotechnical and Geoenvironmental Engineering*, 139(7): 1022–1034.

Rowe, R.K., and Yu, Y. 2013b. Modelling of leachate collection systems with filter-separators in MSW landfills. *ASCE Journal of Environmental Engineering*, 139(8): 1042–1052.

Rowe, R.K., and Yu, Y. 2013c. A practical technique for estimating service life of MSW leachate collection systems. *Canadian Geotechnical Journal*, 50(2): 165–178.

Rowe, R.K., Quigley, R.M., Brachman, R.W.I., and Booker, J.R. 2004. *Barrier systems for waste disposal facilities*. Taylor & Francis Books Ltd. (E & FN Spon) London.

Rowe, R.K., Abdelaal, F.B., and Brachman, R.W.I. 2013. Antioxidant depletion from an HDPE geomembrane with a sand protection layer. *Geosynthetics International*, 20(2): 73-89.

Rowe, R.K., Brachman, R.W.I, Take, W.A, Rentz, A., and Ashe, L.E. 2016. Field and laboratory observations of down-slope bentonite migration in exposed composite liners. *Geotextiles and Geomembranes*, 44(5): 686-706.

Rowe, R.K., Brachman, R.W.I., Hosney, M.S., Take, W.A., and Arnepalli, D.N. 2017. Insight into hydraulic conductivity testing of GCLs exhumed after 5 and 7 years in a cover. *Canadian Geotechnical Journal*, 54(8): 1118-1138.

Saheli, P.T., and Rowe, R.K. 2016. Diffusive Transport of Bisphenol-A (BPA) through a Geosynthetic Clay Liner (GCL). *Geotextiles and Geomembranes*, 44(5): 731-738.

Saheli, P.T., Rowe, R.K., Petersen, E.J., and O'Carroll, D.M. 2017. Diffusion of multiwall carbon nanotubes (MWCNTs) through a high density polyethylene (HDPE) geomembrane. *Geosynthetics International*, 24(2): 184-197.

Schofield, A.N. 1980. Cambridge geotechnical centrifuge operation. *Géotechnique*, 30(3): 227–268.

Selig, E.T. 1988. Soil parameters for design of buried pipelines. *In Proceedings of the Conference of Pipeline Infrastructure*, B.A. Bennet, Editor, American Society of Civil Engineers (ASCE), Reston, VA, 99–116.

Setz, M.C., Tian, K., Benson, C.H., and Bradshaw, S.L. 2017. Effect of ammonium on the hydraulic conductivity of geosynthetic clay liners. *Geotextiles and Geomembranes*, 45(6): 665-673.

Shackelford, C.D., Meier, A., and Sample-Lord, K. 2016. Limiting membrane and diffusion behavior of a geosynthetic clay liner. *Geotextiles and Geomembranes*, 44(5): 707-718.

Sia, A.H.I., and Dixon, N. 2012. Numerical modelling of landfill lining system-waste interaction: implications of parameter variability. *Geosynthetics International*, 19(5): 393-408.

Taylor, R.N. 1995. *Geotechnical Centrifuge Technology,* Blackie Academic and Professional, Glasgow, U.K.

Thusyanthan, N.I., Madabhushi, S.P.G., and Singh, S. 2007. Tension in geomembranes on landfill slopes under static and earthquake loading - Centrifuge study. *Geotextiles and Geomembranes*, 25(2): 78-95.

Touze-Foltz, N., Bannour, H., Barral, C., and Stoltz, G. 2016. A review of the performance of geosynthetics for environmental protection. *Geotextiles and Geomembranes*, 44(5): 656-672.

Villard, P., Gourc, J.P., and Feki, N. 1999. Analysis of geosynthetic lining system (GLS) undergoing large deformations. *Geotextiles and Geomembranes*, 17(1): 17-32.

Wu, X. 2013. Effect of waste settlement and seismic loading on the integrity of geosynthetic barrier systems. Masters' thesis, School of Sustainable Engineering and the Built Environment, Arizona State University, Tempe, Arizona, USA.

Yang, P., Xue, S.B., Song, L., and Zhu, X.W. 2017. Numerical simulation of geomembrane wrinkle formation. *Geotextiles and Geomembranes*, 45(6): 697-701.

Yu, Y., and Bathurst, R.J. 2017. Influence of selection of soil and interface properties on numerical results of two soil-geosynthetic interaction problems. *ASCE International Journal of Geomechanics*, 17(6): 04016136.

Yu, Y., Bathurst, R.J., and Allen, T.M. 2016. Numerical modelling of the SR-18 geogrid reinforced modular block retaining walls. *ASCE Journal of Geotechnical and Geoenvironmental Engineering*, 142(5): 04016003.

Yu, Y., and Rowe, R.K. 2012. Modelling leachate-induced clogging of porous media. *Canadian Geotechnical Journal*, 49(8): 877–890.

Yu, Y., and Rowe, R.K. 2013. Effect of grain size on service life of MSW landfill drainage systems. *Canadian Geotechnical Journal*, 50(1): 1–14.

Zeng, X., and Lim, S.L. 2002. The influence of variation of centrifugal acceleration and model container size on accuracy of centrifuge test. *Geotechnical Testing Journal*, 25(1): 24–43.

Zamara, K.A., Dixon, N., Fowmes, G., Jones, D.R.V., and Zhang, B. 2014. Landfill side slope lining system performance: A comparison of field measurements and numerical modelling analyses. *Geotextiles and Geomembranes*, 42(3): 224-235.

Figure Captions

Figure 1. Centrifuge model geometry (based on Kavazanjian and Gutierrez 2017).

Figure 2. Prototype geometry and FLAC numerical grid.

Figure 3. Calculated and measured stress-strain response of foundation (cemented sand) from triaxial compression tests.

Figure 4. Calculated and measured stress-strain response of foundation (cemented sand) from one-dimensional compression tests.

Figure 5. Calculated and measured stress-strain response of waste (sand-peat mixture with 3:1 by mass) from one-dimensional compression test.

Figure 6. Geomembrane (PFSA membrane) tensile load-strain relationship. Note: PFSA membrane tensile strength and stiffness under 60g in the prototype are $T_y = 2.0 \times 60 = 120$ kN/m and $J = 33.33 \times 60 = 2000$ kN/m, respectively.

Figure 7. Initial and calculated final prototype geometry using base case parameter values and FLAC large-strain mode. Note: At prototype scale, the measured surface settlement at the landfill centre was 4.2 m (Kavazanjian and Gutierrez 2017); the calculated maximum surface settlement was 4.7 m at the landfill top surface vertically above the centre of the landfill base; the calculated surface settlement at the centre of the landfill top surface was 4.5 m.

Figure 8. Distribution of PFSA membrane tensile loads and strains from the FLAC model using base case parameters and large-strain mode.

Figure 9. PFSA membrane (a) tensile loads and (b) tensile strains calculated using base case parameters and large-strain mode. Measured tensile strains are from Kavazanjian and Gutierrez 2007).

Figure 10. Influence of foundation (cemented sand) parameter values on PFSA membrane (a) tensile loads and (b) tensile strains.

Figure 11. Influence of interface shear strength between PFSA membrane and foundation (cemented sand) on PFSA membrane (a) tensile loads and (b) tensile strains.

Figure 12. Influence of interface shear stiffness on PFSA membrane (a) tensile loads and (b) tensile strains.

Figure 13. Influence of interface shear and normal stiffness on PFSA membrane (a) tensile loads and (b) tensile strains.

Figure 14. Influence of FLAC large- and small-strain mode on PFSA membrane (a) tensile loads and (b) tensile strains.

Table 1. Parameter values of foundation (cemented sand).

Property	Value
Density, ρ_f (kg/m^3)	1660
Nonlinear elastic-plastic model [a]	
Elastic modulus number, K_e (-)	440
Unloading-reloading modulus number, K_{ur} (-)	528
Elastic modulus exponent, n (-)	0.40
Failure ratio, R_f (-)	0.95
Initial tangent bulk modulus number, B_i/p_a (-)	48.3
Asymptotic volumetric strain value, ε_u (-)	0.06
Tangent Poisson's ratio, v_t (-)	0−0.49
Friction angle, ϕ_f (°)	34
Cohesion, c_f (kPa)	28
Dilation angle, ψ_f (°)	0
Atmospheric pressure, p_a (kPa)	101.3

Note:

[a] Selected parameter values are based on the sandy silt reported by Boscardin et al. (1990) with the similar stress-strain relationship as the cemented sand used by Kavazanjian and Gutierrez (2017).

Table 2. Parameter values of waste (sand-peat mixture with 3:1 by mass).

Property	Value
Density, ρ_w(kg/m^3)	830
Modified Cam-Clay model	
Maximum elastic bulk modulus, K_{max} (MPa)	100
Poisson's ratio, v (-)	0.33
Frictional constant, M (-)	1.2
Slope of normal consolidation line, λ (-)	0.18
Slope of elastic swelling line, κ (-)	0.05
Reference pressure, p_1 (kPa)	1
Pre-consolidation stress, p_c (kPa)	10
Specific volume at reference pressure on normal consolidation line [a], υ_λ (-)	3.34

Note:
[a] Based on initial void ratio e_0 = 2.0 and initial effective pressure p_0 = 2.4 kPa.

Table 3. Geomembrane (PFSA membrane) parameter values in the prototype using FLAC beam elements.

Beam element parameters	Value
Axial stiffness, J (kN/m)	2000
Moment of inertia, I (m^4)	0
Tensile strength, T_y (kN/m)	120
Young's modulus [a], E_g (MPa)	667
Cross-sectional area [b], A_g (m^2/m)	3×10^{-3}
Peak tensile yield strength [c] S_y (MPa)	40
Residual tensile yield strength, S_{yr} (MPa)	40

Notes:
[a] $E_g = J/A_g$;
[b] Based on 3-mm thick product per meter out-of-plane direction;
[c] $S_y = T_y/A_g$.

Table 4. Interfaces and corresponding parameter values for the base case.

Interface and parameters	Value
Normal stiffness, k_n (MPa/m)	100
Shear stiffness, k_s (MPa/m)	1
Dilation angle, ψ_i (°)	0
Cohesion, c_i (kPa)	0
PFSA membrane-waste (sand peat mixture)	
Friction angle, ϕ_{gw} (°)	27
PFSA membrane-foundation (cemented sand)	
Friction angle, ϕ_{gf} (°)	29
PFSA membrane-LDPE membrane	
Friction angle, ϕ_{gg} (°)	0

Table 5. Initial parameter values of foundation (cemented sand) and waste (sand-peat mixture with 3:1 by mass).

Property	Value
Foundation (cemented sand) elastic model [a]	
Young's modulus, E_f (MPa)	30
Poisson's ratio, ν_f (-)	0.3
Waste (sand-peat mixture) elastic model [b]	
Young's modulus, E_w (MPa)	2
Poisson's ratio, ν_w (-)	0.33
Waste (sand-peat mixture) Mohr-Coulomb model [c]	
Friction angle, ϕ_w (°)	30
Cohesion, c_w (kPa)	5
Dilation angle, ψ_w (°)	0

Note:
[a] Used to set up the initial stresses within the foundation;
[b] Used to set up the initial stresses within the waste;
[c] Used to remove the tensile mean stresses before applying the Cam-Clay model to the waste.

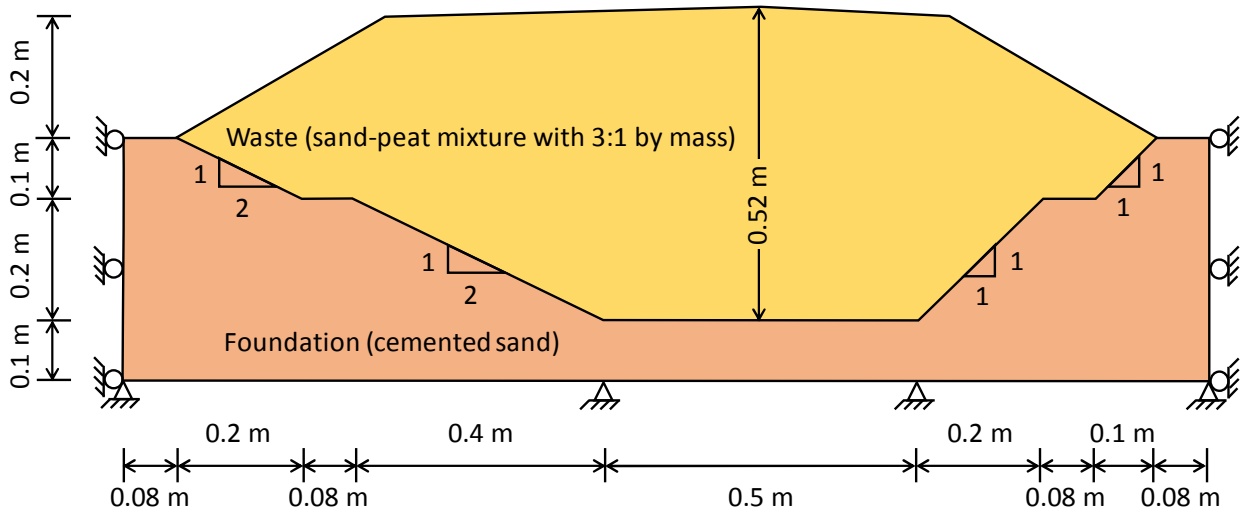

Figure 1. Centrifuge model geometry (based on Kavazanjian and Gutierrez 2017).

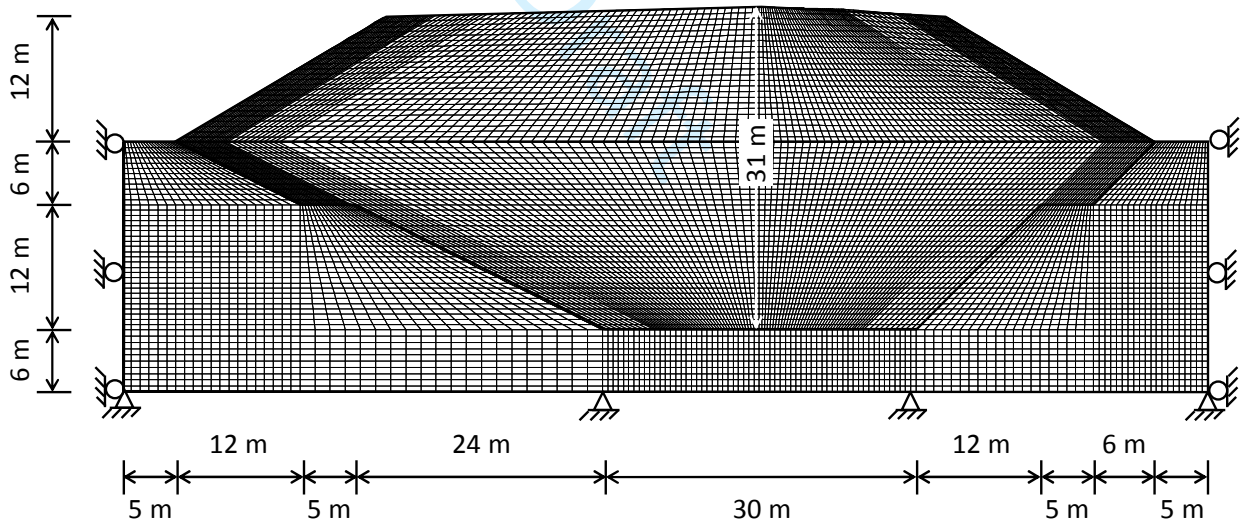

Figure 2. Prototype geometry and FLAC numerical grid.

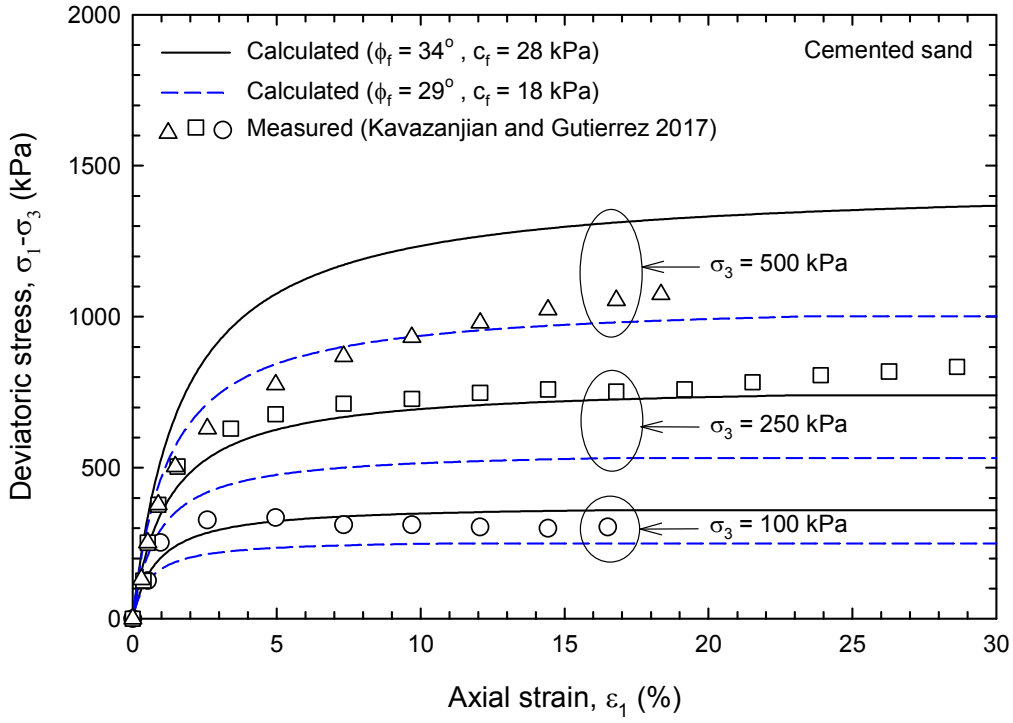

Figure 3. Calculated and measured stress-strain response of foundation (cemented sand) from triaxial compression tests.

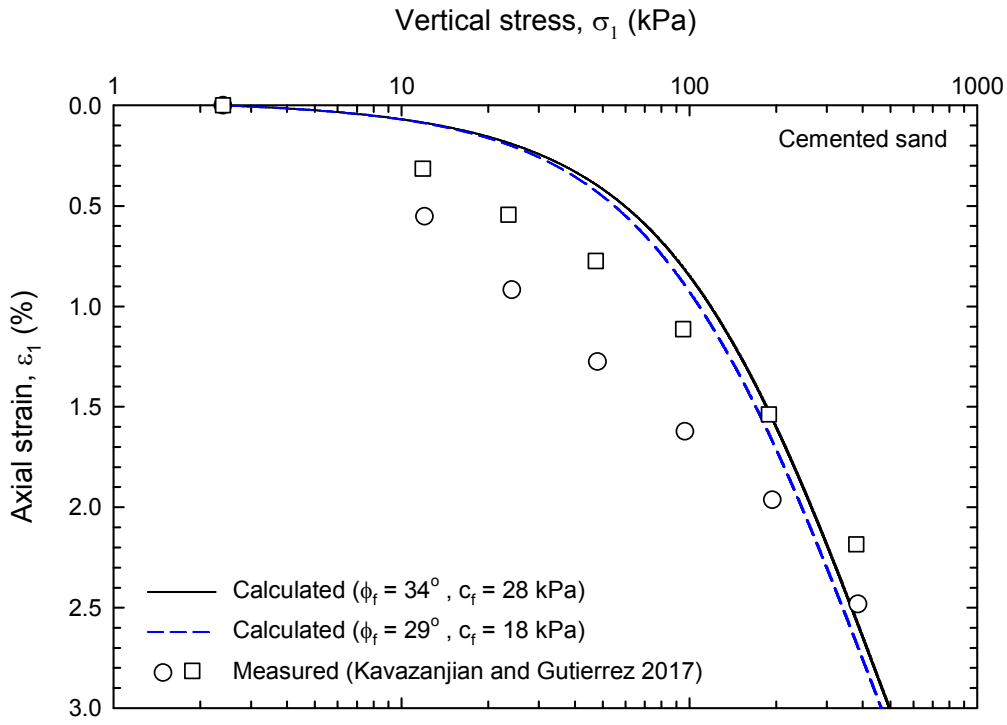

Figure 4. Calculated and measured stress-strain response of foundation (cemented sand) from one-dimensional compression tests.

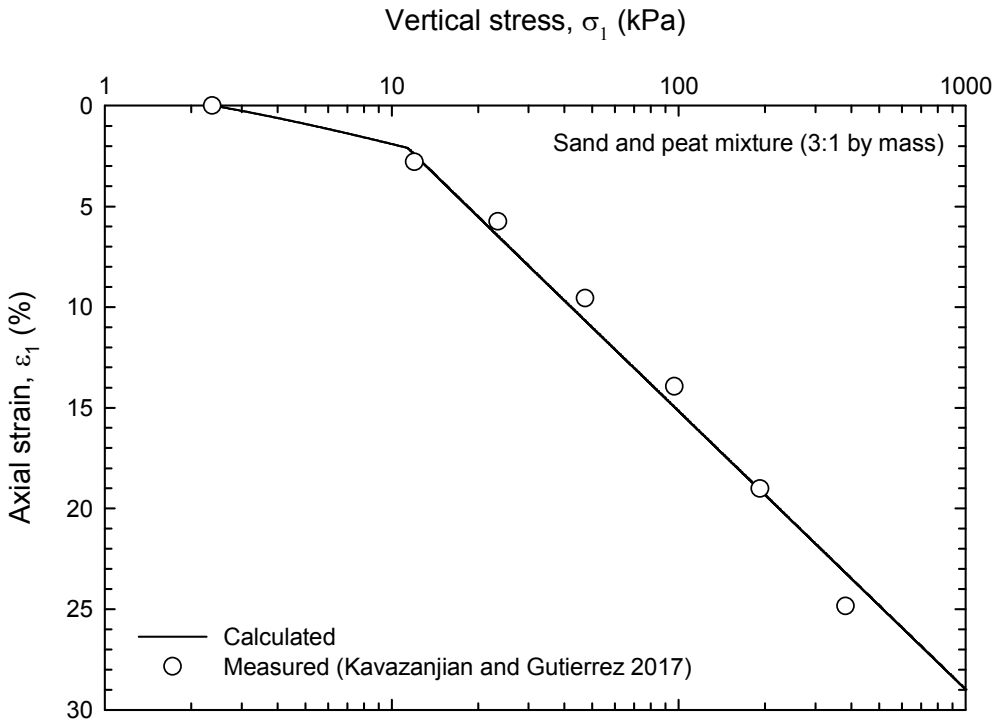

Figure 5. Calculated and measured stress-strain response of waste (sand-peat mixture with 3:1 by mass) from one-dimensional compression test.

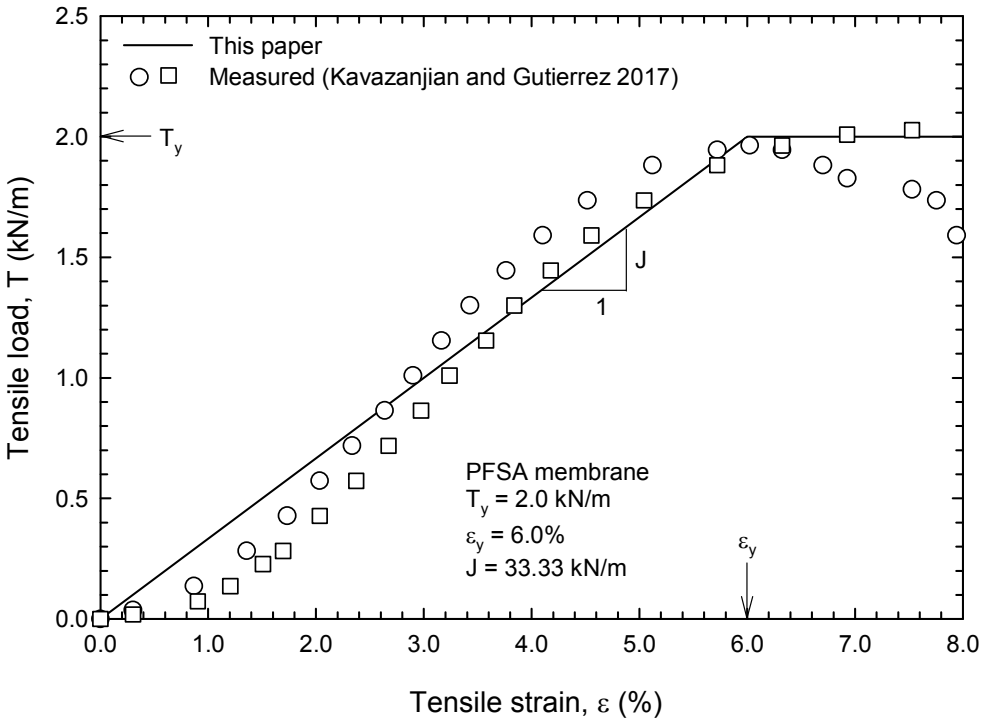

Figure 6. Geomembrane (PFSA membrane) tensile load-strain relationship. Note: PFSA membrane tensile strength and stiffness under 60g in the prototype are $T_y = 2.0 \times 60 = 120$ kN/m and $J = 33.33 \times 60 = 2000$ kN/m, respectively.

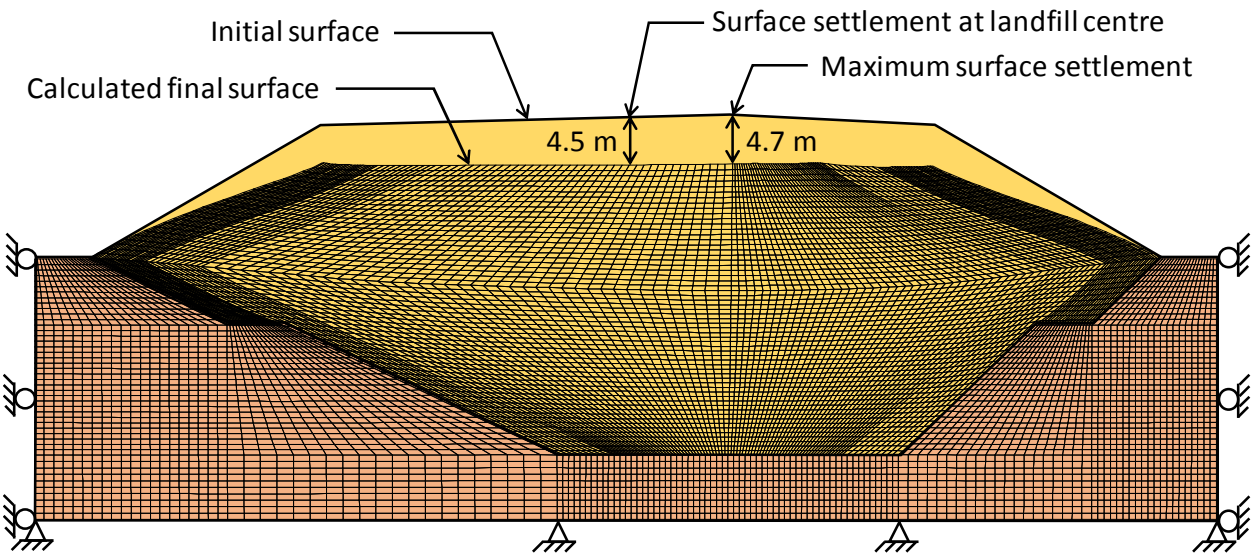

Figure 7. Initial and calculated final prototype geometry using base case parameter values and FLAC large-strain mode. Note: At prototype scale, the measured surface settlement at the landfill centre was 4.2 m (Kavazanjian and Gutierrez 2017); the calculated maximum surface settlement was 4.7 m at the landfill top surface vertically above the centre of the landfill base; the calculated surface settlement at the centre of the landfill top surface was 4.5 m.

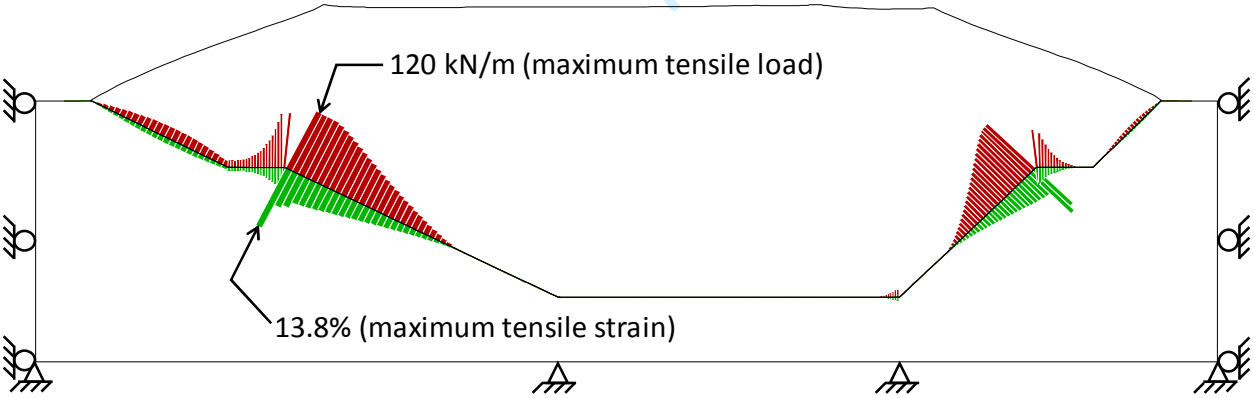

Figure 8. Distribution of PFSA membrane tensile loads and strains from the FLAC model using base case parameters and large-strain mode.

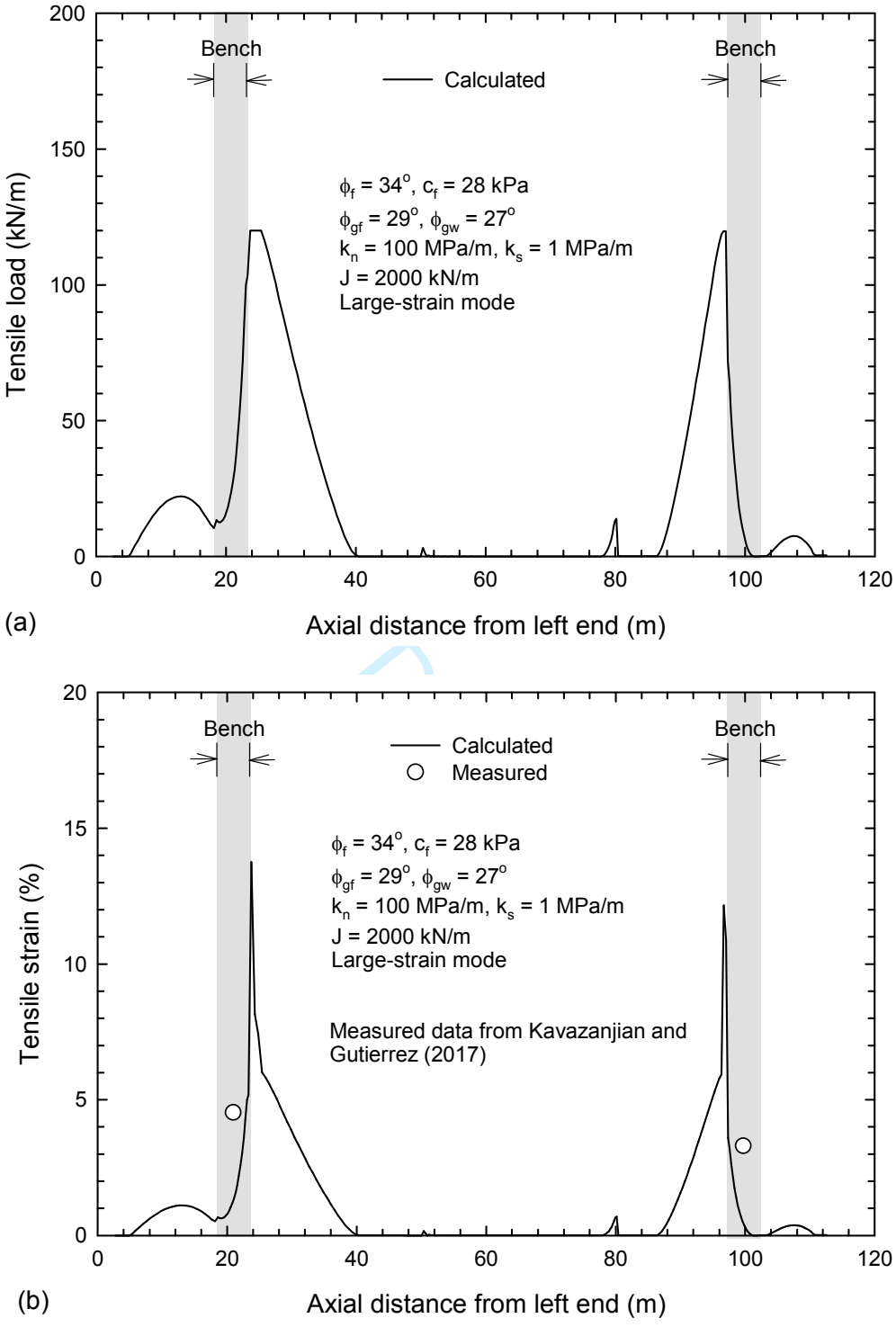

Figure 9. PFSA membrane (a) tensile loads and (b) tensile strains calculated using base case parameters and large-strain mode. Measured tensile strains are from Kavazanjian and Gutierrez 2007).

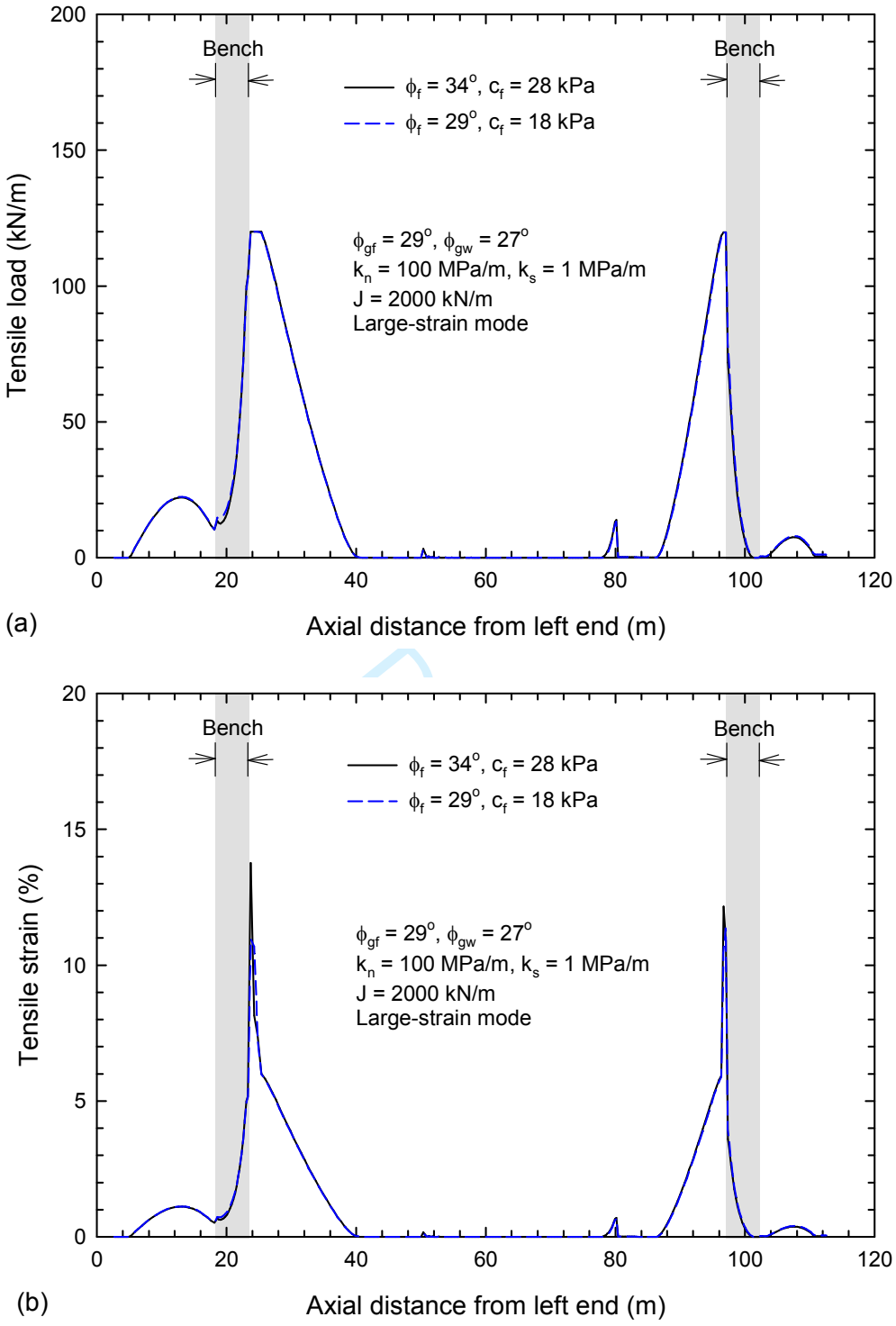

Figure 10. Influence of foundation (cemented sand) parameter values on PFSA membrane (a) tensile loads and (b) tensile strains.

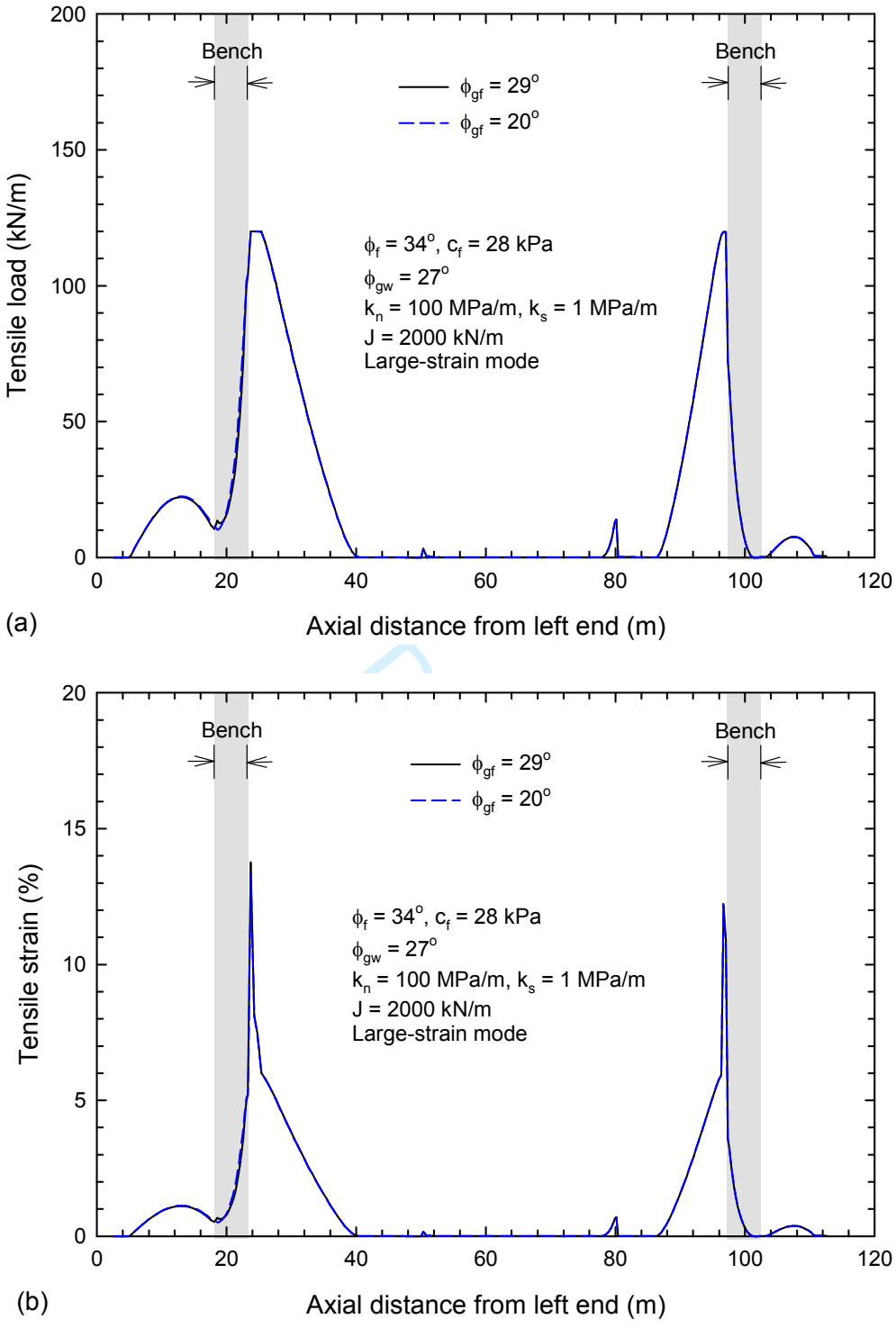

Figure 11. Influence of interface shear strength between PFSA membrane and foundation (cemented sand) on PFSA membrane (a) tensile loads and (b) tensile strains.

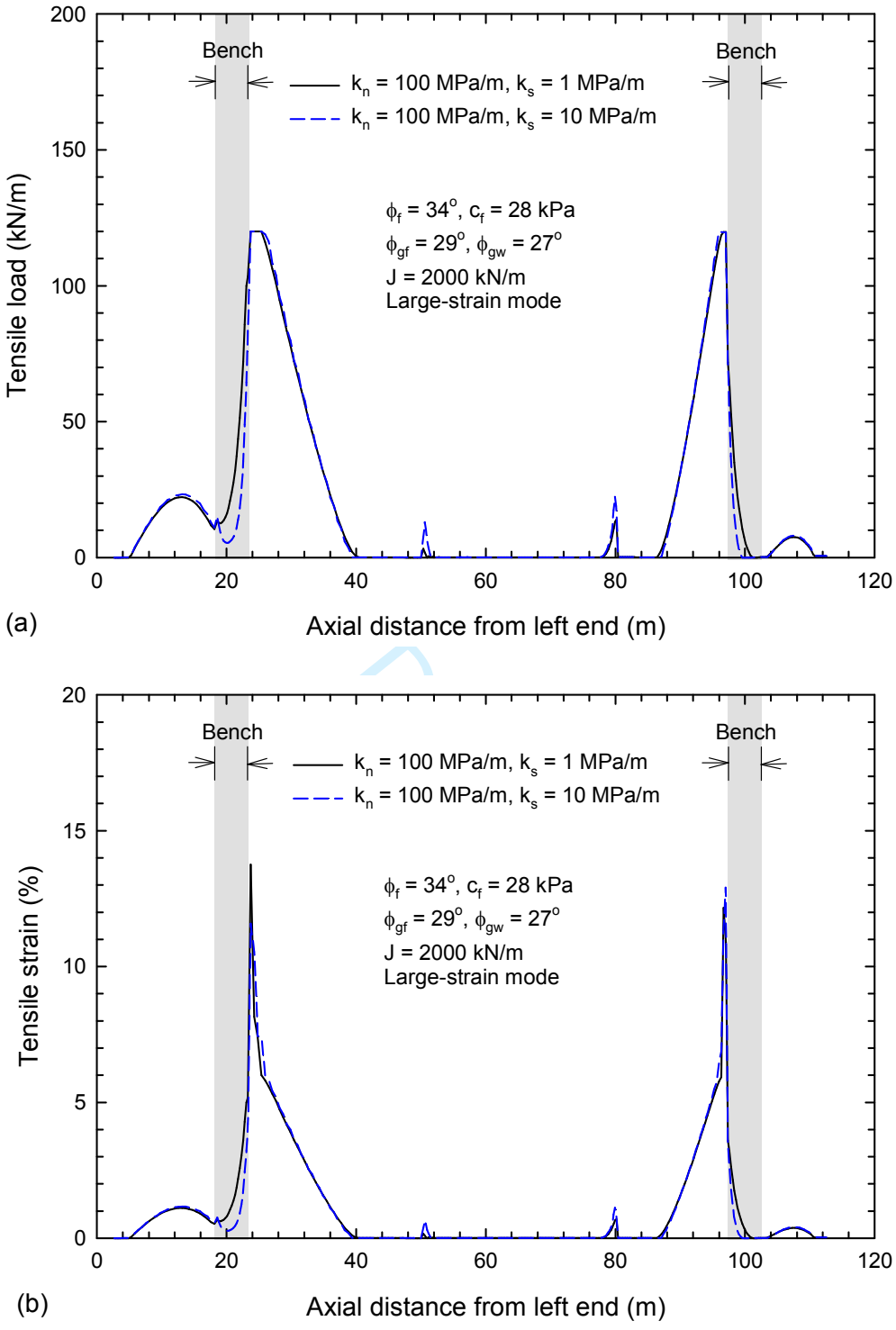

Figure 12. Influence of interface shear stiffness on PFSA membrane (a) tensile loads and (b) tensile strains.

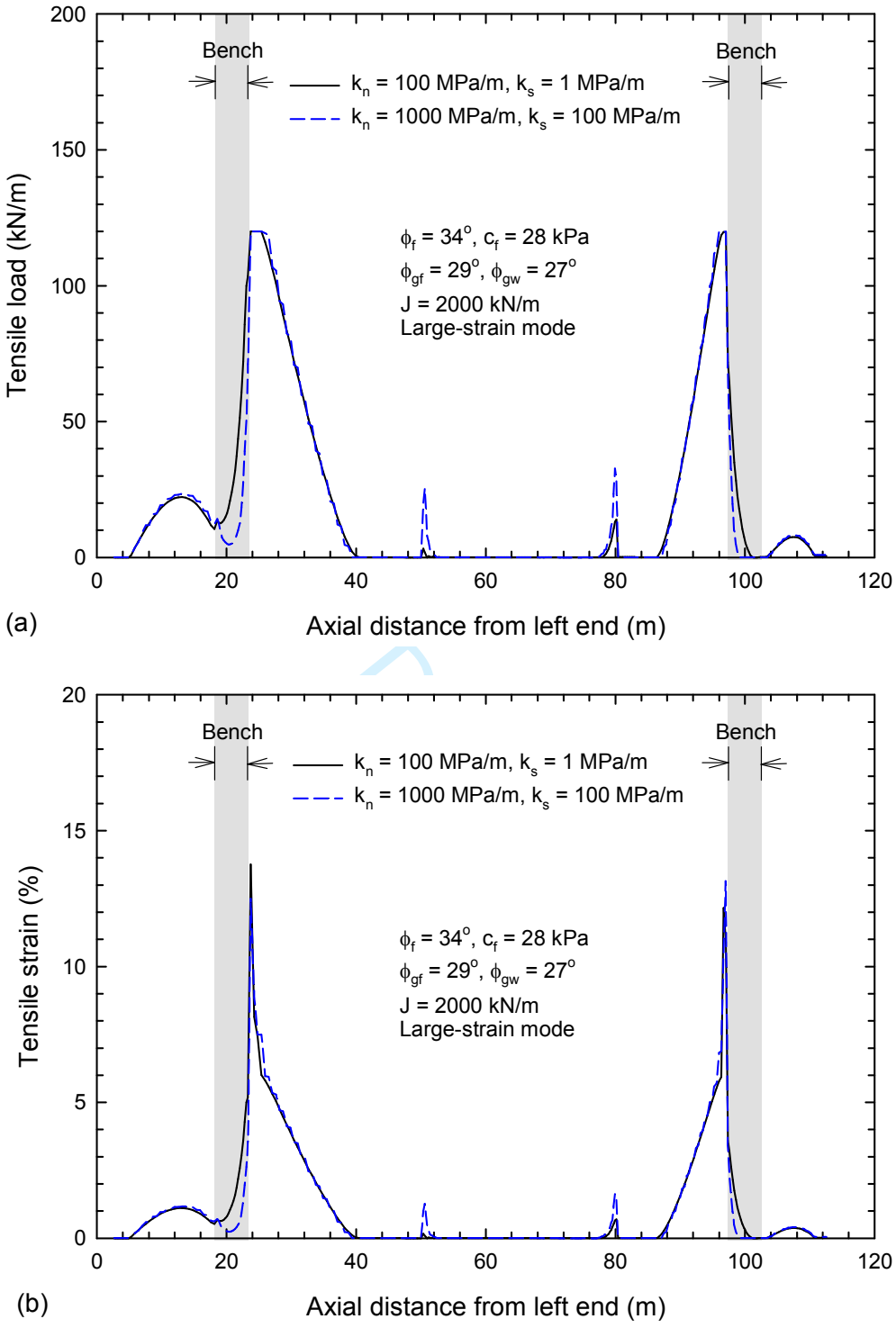

Figure 13. Influence of interface shear and normal stiffness on PFSA membrane (a) tensile loads and (b) tensile strains.

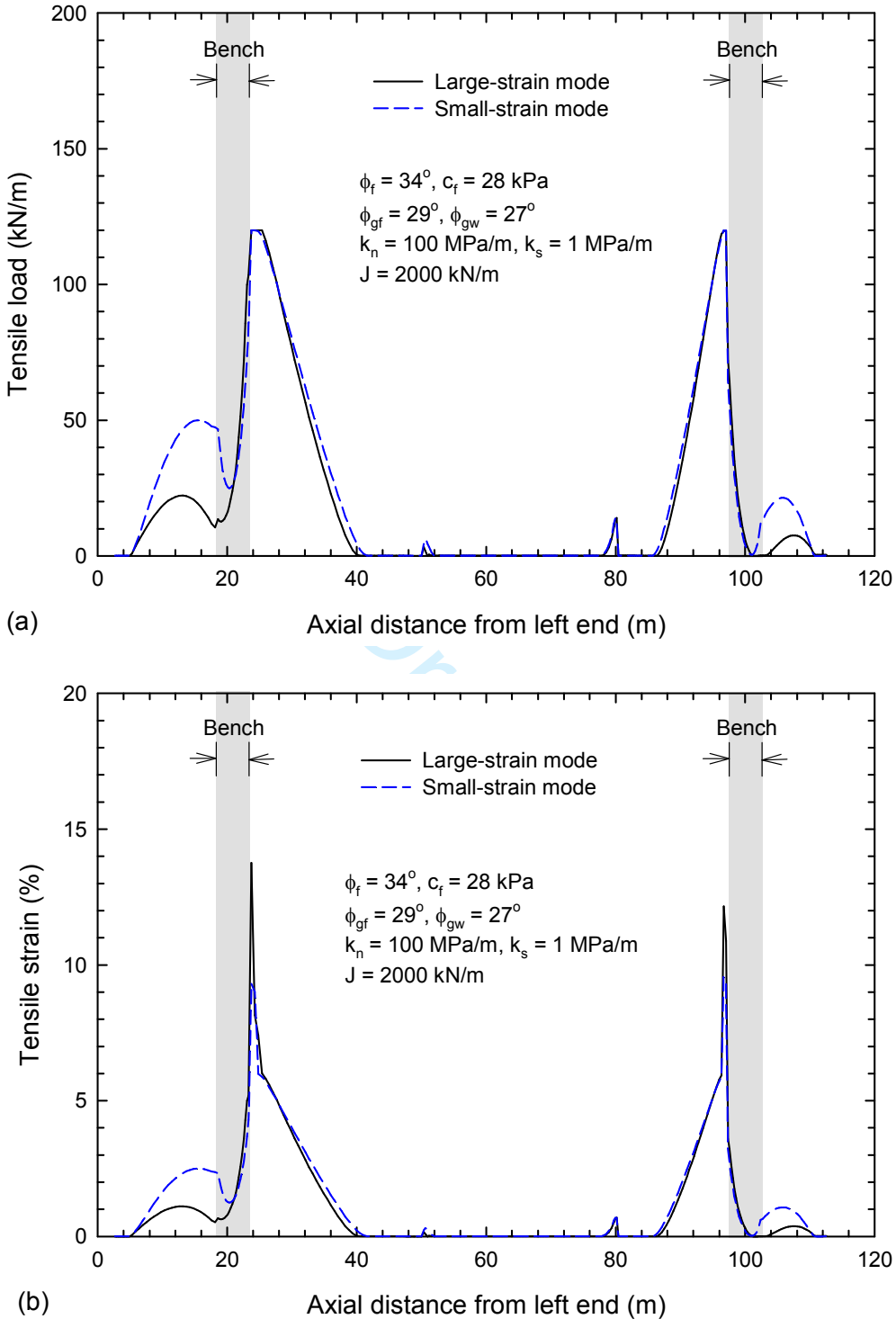

Figure 14. Influence of FLAC large- and small-strain mode on PFSA membrane (a) tensile loads and (b) tensile strains.